Energy & Environmental Science

ROYAL SOCIETY OF CHEMISTRY

PAPER

View Article Online
View Journal

Cite this: DOI: 10.1039/d4ee01755b

Interfacial degradation of silicon anodes in pouch cells†

Qiu Fang,[ab] Shiwei Xu,[ac] Xuechao Sha,[d] Di Liu,[d] Xiao Zhang,[ab] Weiping Li,[ab] Suting Weng,[ac] Xiaoyun Li,[ab] Liquan Chen,[a] Hong Li,[abcg] Bo Wang,[ef]* Zhaoxiang Wang[abc]* and Xuefeng Wang[abc]*

Received 22nd April 2024,
Accepted 22nd July 2024

DOI: 10.1039/d4ee01755b

rsc.li/ees

The practical application of silicon (Si) anodes in the next-generation high-energy lithium-ion batteries (LIBs) is largely hindered by their capacity loss due to the formation of a solid electrolyte interphase (SEI). Although much work has been carried out to investigate the interfacial evolution of Si, most of them focused on nanostructured Si cycled in coin cells or customer-designed cells, whose working conditions are far from practical usage. Herein, the capacity degradation mechanism and associated interfacial evolution of the micro-sized Si particles cycled in pouch cells are uncovered through multi-scale imaging and spectroscopy techniques, especially cryogenic electron microscopy (cryo-EM). The results show that the surface of Si particles is gradually corroded by the electrolyte, forming a thick (up to 2.5 μm after 300 cycles) and porous SEI rich in organic carbonates and Li_xSiO_y. After profiling the nanostructure and chemical distribution across it, the porosity of the SEI is determined to be ~53.5% and thus a bottom-up SEI growth mechanism is proposed. To achieve a dense and stable SEI, an elastic SEI with a crosslinking network is used to enhance the interfacial stability of the Si anode. Our findings not only reveal the underlying failure mechanism of the Si anode beneficial for its practical applications but also provide a comprehensive understanding of dynamic interfacial evolution enlightening for future interfacial design to achieve high-performance batteries.

Broader context

Silicon (Si) anodes are considered as some of the promising candidates for Li-ion batteries with higher energy density. However, potential issues, including low conductivity, drastic volume change during lithiation/de-lithiation, particle pulverization and interface instability, hinder the practical application of Si anodes. Interface instability is the most complicated issue since a solid electrolyte interphase (SEI) originates from the reaction between the electrolyte and Si particles and changes as a function of the number of cycles. In this work, techniques from the nanoscale to microscale were integrated to uncover the chemical and structural evolution of an interface on the micro-sized Si particles in pouch cells after different cycles. Our findings not only provide a comprehensive picture of the battery interface evolution, known as the most important but least understood part, but also point out the remaining key problems and future directions to push the practical application of Si anodes.

Introduction

Silicon (Si) with a high specific capacity (3579 mA h g^{-1} for $Li_{15}Si_4$) and low cost is going to be used in the next-generation Li-ion batteries (LIBs) with higher energy density.[1–3] Intense efforts from both academia and industry have been put into recognizing and tackling the potential issues hindering the practical use of Si anodes, such as their low conductivity,[4–6] drastic volume change during lithiation/de-lithiation,[7–9] particle pulverization,[10,11] and interface instability.[9,12,13] The former three issues can be addressed/alleviated by the nanostructure design of Si particles, such as embedding Si nanodots into carbonaceous substances.[14–18] The latter one is complex since it involves a mixture of organic and inorganic products known as solid electrolyte interphases (SEIs), originating from the

[a] Beijing National Laboratory for Condensed Matter Physics, Institute of Physics, Chinese Academy of Sciences, Beijing 100190, China. E-mail: wxf@iphy.ac.cn, zxwang@iphy.ac.cn
[b] College of Materials Science and Opto-Electronic Technology, University of Chinese Academy of Sciences, Beijing 100049, China
[c] School of Physical Sciences, University of Chinese Academy of Sciences, Beijing 100049, China
[d] ZEISS Research Microscopy Solutions, Carl Zeiss (Shanghai) Co. Ltd., Shanghai 200131, China
[e] Watt Lab, Central Research Institute, Huawei Technologies Co., Ltd., Shenzhen 518129, China. E-mail: wangbo19880804@163.com
[f] State Key Laboratory of Space Power-Sources, School of Chemistry and Chemical Engineering, Harbin Institute of Technology, Harbin 150001, China
[g] Tianmu Lake Institute of Advanced Energy Storage Technologies Co. Ltd., Liyang 213300, Jiangsu, China

† Electronic supplementary information (ESI) available. See DOI: https://doi.org/10.1039/d4ee01755b

reaction between the electrolyte and Si particles, and is subject to change as a function of the number of cycles, which requires to uncover its dynamic evolution comprehensively, especially under the practical working conditions.

Attempting to monitor the component and structure evolution of a SEI on the Si anode is very challenging due to its low content, low contrast, and air and radiation sensitivity. Moreover, it continues to grow with the cycling, resulting in its thickness covering from nanometers to micrometers.[19] Guduru applied *in situ* atomic force microscopy (AFM) to measure the SEI thickness on the Si film during the first two cycles and found that the SEI grows primarily during initial lithiation, reaching a thickness of 17–20 nm.[20] Using solid-state nuclear magnetic resonance spectroscopy (ssNMR), Grey revealed that the SEI on the Si nanoparticles (average particle size ~50 nm) grows pronouncedly in the initial 30 cycles (corresponding to 50% state of health) and becomes relatively stable after that, which is dominated by the organic species, such as $ROCO_2Li$ and RCO_2Li.[21] The emerging advanced cryogenic (scanning) transmission electron microscopy (cryo-(S)TEM) enables direct visualization of the SEI at the nanoscale with minimized radiation damage.[22,23] For example, Cui and Wang uncovered the native instability of the SEI on Si nanowires and nanoparticles containing Li_2O and organic carbonates formed during lithiation, which when allowed to react with Si generate amorphous Li_xSiO_y and are oxidized during de-lithiation, respectively.[24,25] After the first lithiation, a core–shell structure forms with an outer SEI layer as shown using cryo-EDS.[26] By integrating elemental tomography, an advanced algorithm, and cryo-STEM, Wang unveiled the progressive growth of the SEI towards the Si interior as the Si nanowires become porous with cycling, eventually evolving into a 'plum-pudding' structure after 100 cycles.[27] Gradual SEI accumulation not only consumes more active Li^+ but also contributes to forming a 'dead' Li_xSi alloy by disrupting the electron conduction pathways, causing fast capacity loss of the Si anode.[25]

However, most previous research studies were carried out based on the nanostructured Si cycled in coin cells or customer-designed cells, and the practical application of micro-sized Si particles in pouch or cylinder cells is far away from realization. This discrepancy will lead to difficulty in directly transferring the knowledge from the fundamental research to the practical application and urgently requires to be eliminated especially when these laboratory-based achievements are going to reach commercialization.[28–30] Although Zhang provided an example of investigating the failure mechanism of a micro-sized Si/C composite anode in pouch cells, their analysis was carried out mainly using electrochemical techniques without probing the interfacial degradation of Si particles deeply,[31] which turned out to be the main cause for the capacity loss of pouch cells. Thus, it is essential to fully understand the interfacial evolution of the micro-sized Si in pouch cells through multiscale techniques.

In this work, various imaging and spectroscopy techniques were integrated to uncover the chemical and structural evolution of an interface on the micro-sized Si particles in pouch cells after different cycles, including cross-section polisher (CP)-scanning electron microscopy (SEM), SEM-Raman microscopy, Fourier transform infrared (FTIR) spectroscopy, cryogenic focus ion beam (cryo-FIB)-cryogenic transmission electron microscopy (cryo-TEM), electron energy loss spectroscopy (EELS), *etc*. Cryo-protection is necessary to minimize beam damage and maintain the intrinsic features. The results show that the surface of Si particles is gradually corroded by the electrolyte, forming a thick and porous SEI rich in organic carbonates and Li_xSiO_y. After 300 cycles, the thickness of the SEI layer reaches about 2.5 μm and the chemical distribution across it was profiled in depth. Based on these observations, the interfacial degradation of the Si anode was pictured including both bottom-up and bottom-down growth mechanisms, and the desirable SEI for the Si anode was proposed to be dense, elastic, and Li^+ conducting. Our findings not only reveal the underlying failure mechanism of Si anodes beneficial for their practical application but also provide a comprehensive understanding of dynamic interfacial evolution enlightening for future interface design to achieve high-performance batteries.

Results and discussion

Si particles used in this work have an average particle size of 3.03 μm (Table S1, ESI†), consisting of crystalline Si nanograins embedded in the carbon substrate with additional 7–8 nm carbon coating (Fig. S1, TEM images, ESI†) for enhanced electronic conductivity and structural stability. Its electrochemical performance (Fig. 1a) was evaluated in pouch cells with a capacity of 450 mA h using $LiCoO_2$ as a cathode, which were cycled under a practical protocol using a combination of galvanostatic and potentiostatic processes as illustrated in Fig. 1b.

The pouch cell shows an initial reversible capacity of 445 mAh and a coulombic efficiency of 96.43% after formation. Although its reversible capacity starts fading slightly from the 150th cycle, a high-capacity retention of 96.63% is achieved after 300 cycles (Fig. 1a), which is better than the state-of-the-art performance of pouch cells based on Si anodes (Table S2 and Fig. S2, ESI†). Nevertheless, voltage profiles at some selected cycles (Fig. 1b) show that the charging voltage during the initial galvanostatic charging process at a voltage range of 3.00–4.10 V gradually decreases especially from the 10th cycle to the 100th cycle, indicating the increased cell polarization by about 0.1 V. Consequently, more charge capacity is delivered at a voltage lower than 4.10 V, and its contribution to the total charge capacity increases from 33% at the 2nd cycle to 49% at the 300th cycle (Fig. 1c). Electrochemical impedance spectra (EIS) of pouch cells after different cycles (Fig. 1d) exhibit aggravating cell resistance from 0.4 Ω after 10 cycles to 0.6 Ω after 300 cycles. Further decoupling the cell resistance by the distribution of relaxation time (DRT) (Fig. 1e and Table S3, ESI†) demonstrates the growing resistance of Li^+ transport through the SEI (A1 in Fig. 1e) from 0.041 Ω (after 10 cycles) to 0.066 Ω (after 300 cycles), as well as the charge transfer at the anode side,[32] which indicate the potential degradation of the Si anode after long cycles while the $LiCoO_2$ cathode remains almost unchanged (Fig. S3, ESI†). Therefore, it is necessary to probe the structural change of the Si anode as a

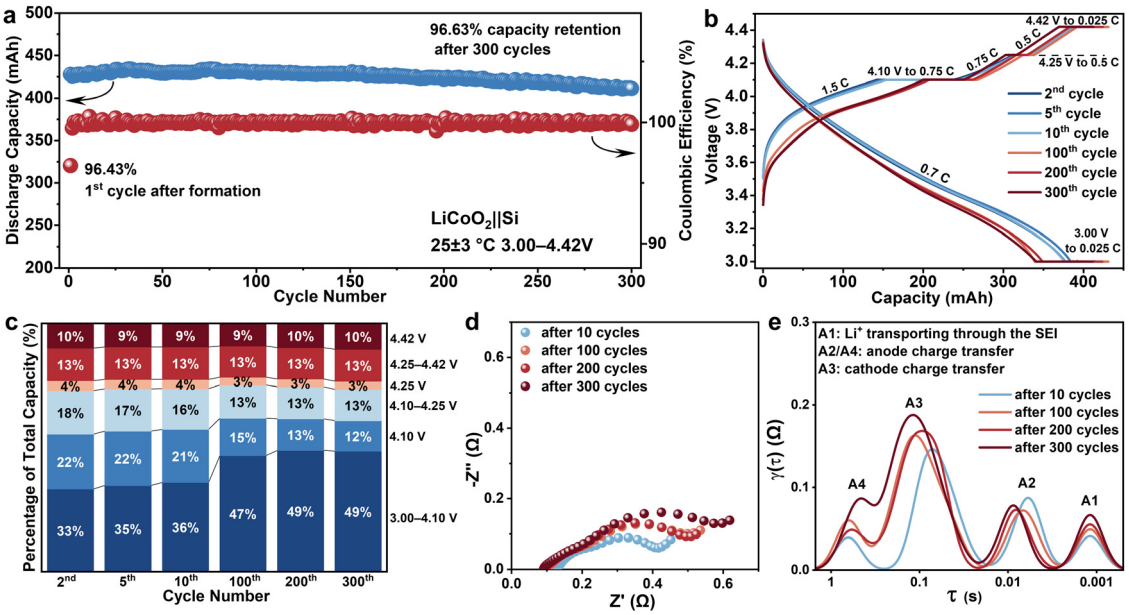

Fig. 1 Electrochemical performance of 450 mA h $LiCoO_2$||Si pouch cells. (a) Cycling performance after formation, (b) voltage profiles at selected cycles, and (c) corresponding charge capacity contribution at the 2nd, 5th, 10th, 100th, 200th, and 300th cycles. (d) EIS spectra of the cells after 10, 100, 200, and 300 cycles and (e) the corresponding spectra as a function of relaxation time after DRT analysis.

function of cycles to uncover its underlying degradation mechanism.

Electrode-scale evolution

To directly visualize the morphology changes of the Si anode, CP technique was applied to mill Si electrodes after different cycles and cross-sectional SEM images were obtained (Fig. 2). After cycles, the thickness of the Si electrode gradually expands from 25 μm (pristine sample, Fig. 2a) to 37 μm after formation (Fig. 2b), then to 46 μm after 10 cycles (Fig. 2c), to 50 μm after 100 cycles (Fig. S4a, ESI†), to 53 μm after 200 cycles (Fig. S4b, ESI†) and 55 μm after 300 cycles (Fig. 2d), which suggest that large volume expansion (by 184%) occurs dominantly during the initial 10 cycles. Meanwhile, the average particle size of Si increased from 3.03 μm to 3.23 μm after formation, to 3.55 μm after 10 cycles, to 3.82 μm after 100 cycles, to 3.92 μm after 200 cycles, and to 4.04 μm after 300 cycles (Table S1, ESI†). The stacking of Si particles in the electrode becomes looser after cycles and large gaps emerge among the particles, which not only separates Si particles from intimate contact but also hinders fast charge transfer from active materials to the current collector, resulting in the increased cell resistance and formation of a 'dead' Li_xSi alloy.[33,34]

Although there are no visible cracks in the single particle, its surface is subjected to continuous corrosion (Fig. 2e–h and Fig. S4c, d, ESI†), forming a porous interface up to 2.5 μm in thickness. Based on element mapping (Fig. 2i–k) and line scanning results (Fig. 2l) acquired by energy dispersive spectroscopy (EDS), this interface is found to consist of C, F, P, S, and O, which are potential reaction products of the interface between the electrolyte and Si known as the SEI. Notably, F is rich in the subsurface (Fig. 2l), which is supposed to form during the early stage of cycling and excludes the possibility that HF corrodes the Si particles.[35] Instead, due to the porous nature of the SEI, the electrolyte is likely to continue to penetrate through the interface and react with the Si bulk.

To study the chemical distribution along the interface, Raman spectroscopy combined with SEM was employed, which allows imaging and probing at the same position (Fig. 2m–o). Line scanning measurements were carried out on the cross-section of Si particles after 300 cycles (Fig. 2n). The signal from amorphous Si at $\sim$459 cm^{-1} is apparent in the bulk (Fig. 2o, labeled as Si bulk) and gradually fades along the interface while a weak peak at $\sim$980 cm^{-1} emerges at the internal surface close to the Si bulk (Fig. 2o, point 3), which is ascribed to lithium silicates (Li_xSiO_y, *e.g.* Li_2SiO_3)[36] originated from the side reaction between Si and Li_2O.[37,38] In addition, the intensity ratio of the D band (at $\sim$1360 cm^{-1}) to the G band (at $\sim$1585 cm^{-1}) from carbonaceous materials gradually decreases from the bulk (Fig. 2o, point 1) to the surface (Fig. 2o, points 5–6), suggesting the enhanced ordering of graphitization as well as the electrical conductivity. This result contradicts the common sense view of the SEI that it is ionically conductive and electrically insulative but agrees with the recent work showing the electrical conductance of a SEI by *in situ* bias TEM.[39] If a SEI can conduct electrons, the electrolyte will be continuously decomposed on the surface leading to aggressive SEI growth.

Since a thick SEI is formed on the Si particle after cycles, Fourier transform infrared spectroscopy–attenuated total reflectance (FTIR-ATR) was carried out to identify the potential functional groups and components in it (Fig. 3). As shown in Fig. 3a, organic species with FTIR absorption bands characteristic of C=O stretching in the 1680–1870 cm^{-1} range and C–H bending and COO^- stretching in the 1250–1500 cm^{-1} range[40]

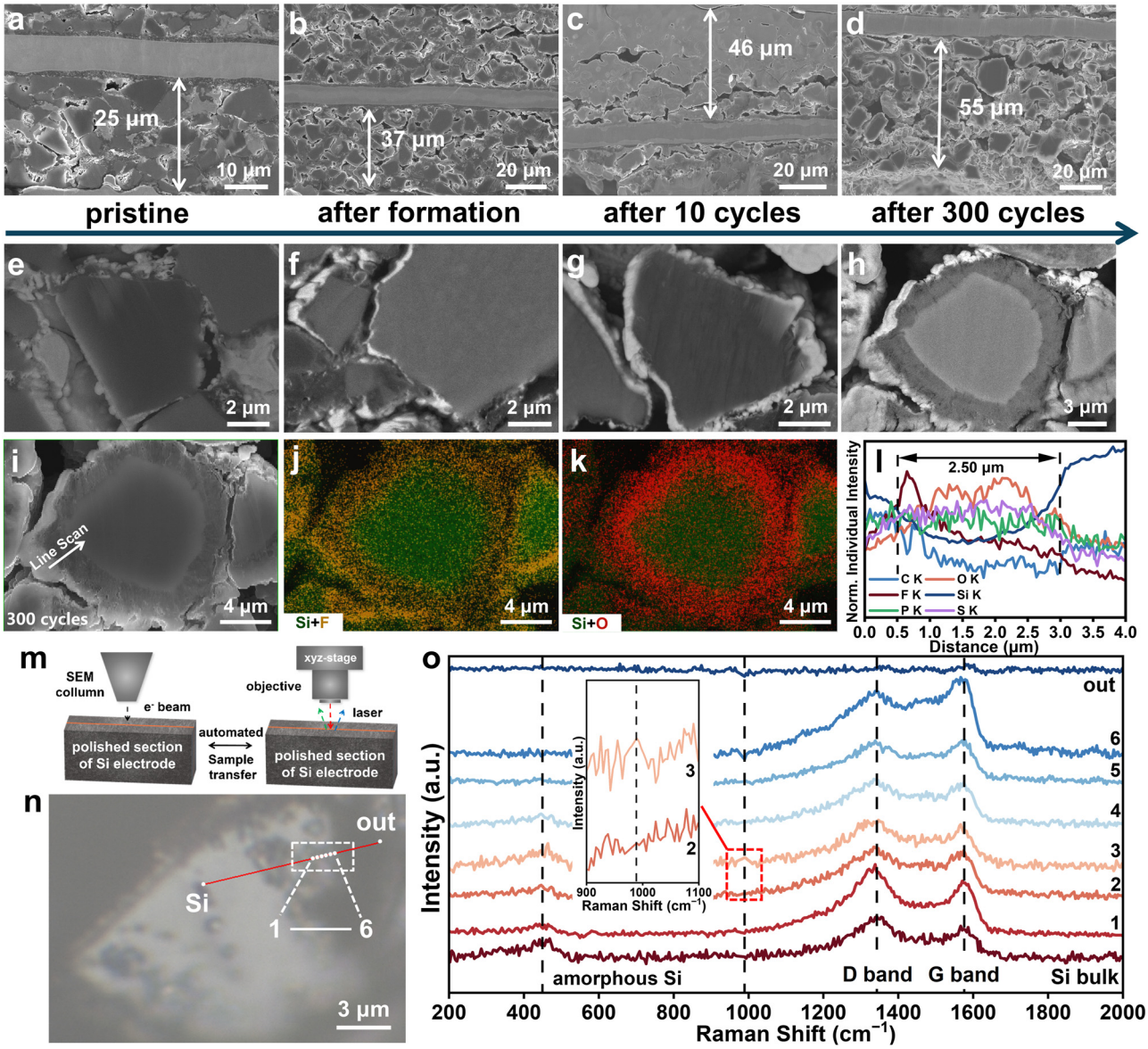

Fig. 2 Morphology change of the Si electrode at different cycles. (a)–(d) Cross-sectional images and (e)–(h) magnified images of the (a) and (e) pristine Si electrode, (b) and (f) after formation, (c) and (g) after 10 cycles, and (d) and (h) after 300 cycles. (i)–(k) Elemental maps and (l) line scanning curve based on EDS. (m) Schematic illustration of the SEM–Raman analysis. (n) Optical image showing the cross-section of a single Si particle after 300 cycles and (o) Raman spectra acquired along its surface with the inset image showing the magnified region from 900 to 1100 cm^{-1}.

appear after formation and their intensity is gradually enhanced with cycles. Meanwhile, a similar trend is found in silicates with Li–Si–O stretching in the 700–1200 cm^{-1} range. It is worth noting that the band at 1079 cm^{-1} belonging to Li_4SiO_4[41] shows growing intensity with increasing cycles, which is much higher than that at 1010 cm^{-1} belonging to Li_2SiO_3/Li_2SiO_5,[42] suggesting that more and more Li ions have been trapped in the silicates.

For more accurate quantitative analysis, an external standard with the same content of additional $LiBF_4$ was introduced during FTIR-ATR measurement (Fig. 3c) since $LiBF_4$ is chemically stable against the cycled electrode and has one dominant characteristic vibration band of B–F stretching at ~1042 cm^{-1} (Fig. 3b).[43] All the spectra were normalized based on the B–F band at 1042 cm^{-1} (Fig. 3d) and magnified as shown in Fig. 3e. It is apparent that the FTIR signals from both organic species and lithium silicates gradually increase as a function of cycle numbers, demonstrating the continuous side reaction between the electrolyte and Si particles and accumulation of by-products leading to the reduced surface mechanical strength (Fig. S5, ESI†).

Nanoscale profile evolution of the SEI

Top surface of the SEI. Given that the detection depth of X-ray photoelectron spectroscopy (XPS) is within 10 nm, it was applied to investigate the chemical bond change on the top surface of the SEI (Fig. S6, ESI†). Consistent with the above FTIR-ATR results, after formation, organic species, Li_2CO_3, and lithium silicates (Li_xSiO_y, at 101.7 eV)[44] are present in the SEI

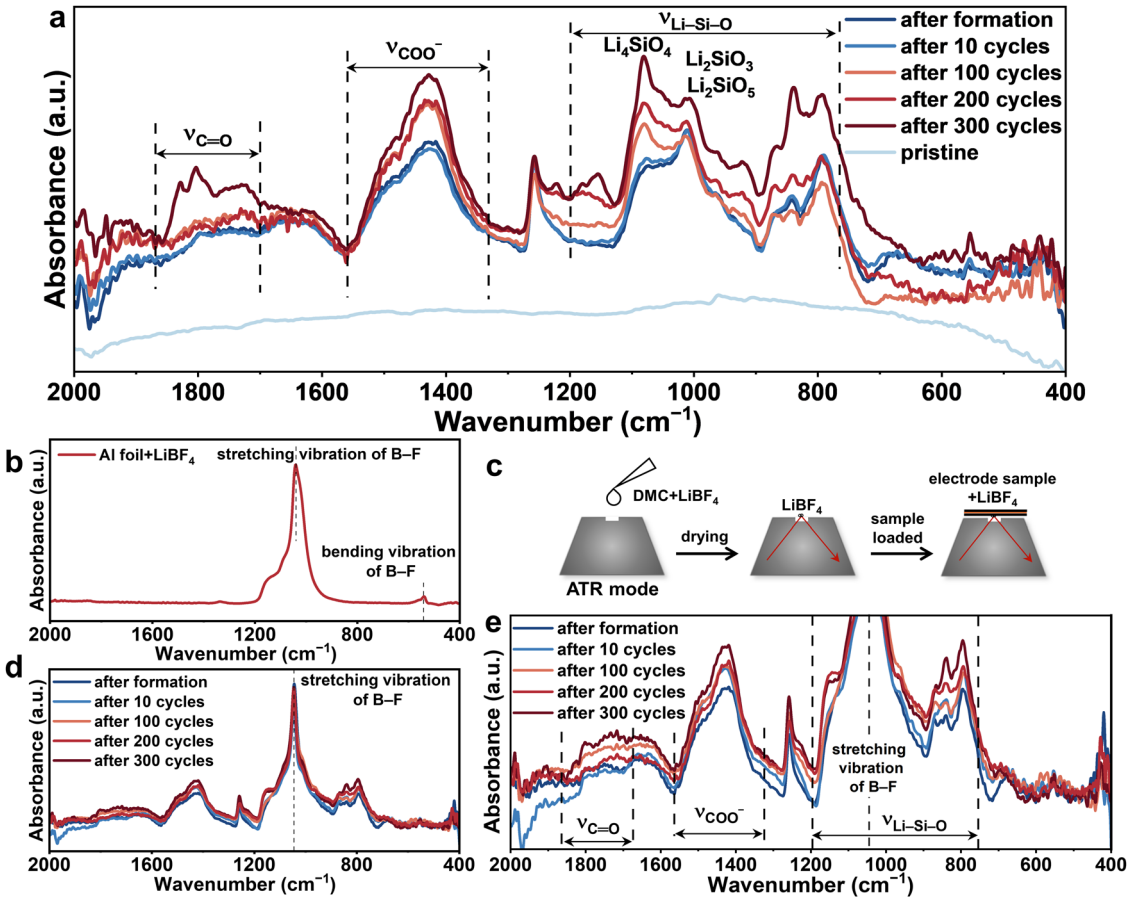

Fig. 3 SEI component evolution probed by FTIR-ATR. (a) FTIR-ATR spectra of Si electrodes after different cycles. (b) FTIR-ATR spectrum of $LiBF_4$. (c) Schematic illustration of adding $LiBF_4$ as an external standard during FTIR-ATR measurement. (d) FTIR-ATR spectra and (e) their corresponding magnified spectra of Si electrodes after different cycles with $LiBF_4$.

since their signals are strong in the C 1s (Fig. S6a, ESI†) and Si 2p spectra (Fig. S6c, ESI†). The absence of a signal for the Si bulk (99.21 eV)[45] indicates that the SEI thickness is larger than 10 nm. Moreover, $LiPF_6$ salt in the electrolyte also decomposes to form LiF, $Li_xPO_yF_z$, and Li_xPF_y, which have peaks at 684.75 eV, 686.45 eV and 687.85 eV, respectively, in the F 1s spectra (Fig. S6b, ESI†).[46] After multiple (>10) cycles, the surface composition of the SEI changes slightly as suggested by their negligible evolution in the XPS spectra, implying the potential bottom-up growth of the SEI.

Bottom layer of the SEI. Cryo-TEM was employed to directly visualize the nanostructure of the SEI close to the Si bulk and EDS was used to distinguish the interface and its thickness (Fig. 4 and Fig. S7–S10, ESI†). After the SEI formation (Fig. 4a and Fig. S7, ESI†), several crystalline Li_2CO_3 and LiF nanograins sporadically disperse in the amorphous organic substance, forming a mosaic structure. Consistent with previous reports,[25] crystalline Li_2O is absent in the SEI, which is likely to react with Si yielding amorphous Li_xSiO_y. After long (>10) cycles, only a few crystalline LiF nanograins are present in the SEI (Fig. 4b–d and Fig. S8–S10, ESI†), which is largely dominated by amorphous organic species and Li_xSiO_y. Based on the elemental distribution of O and Si, the thickness of the interface can be estimated, which is about 8 nm after formation (Fig. 4e), 45 nm after 10 cycles (Fig. 4f), and 55 nm after 100 cycles (Fig. 4g), respectively. However, these values are inclined to be underestimated because of (1) the presence of Li_xSiO_y, and (2) the partial detachment of the SEI especially when it is thick after long cycles. In this regard, line scanning analysis of elemental distribution is helpful to discern the existence of Li_xSiO_y as it shows less Si concentration than the Si bulk (Fig. 4i–l). Thus, the thickness of Li_xSiO_y-containing layers was determined to be about 13 nm after formation (Fig. 4i), 17 nm after 10 cycles (Fig. 4j), 64 nm after 100 cycles (Fig. 4k), and 75 nm after 300 cycles (Fig. 4l), respectively. In this layer, Li_xSiO_y is mixed with other SEI components such as organic species and LiF as shown by the strong EDS signals from C, O, and F (Fig. 4j–l). Besides the Li_xSiO_y-containing layer close to the Si bulk, an external layer is present in the SEI, rich in organic species as suggested by the above high-resolution TEM (HRTEM) images (Fig. 4b–d) and the elemental distribution (Fig. 4j–l). These two layers compose a thick SEI layer with thickness up to hundreds of nanometers (Fig. 4k). Once its thickness becomes >100 nm, it is easy to detach the SEI partially during the sample preparation, leading to the formation of a relatively thin SEI layer after 300 cycles (91 nm, Fig. 4l).

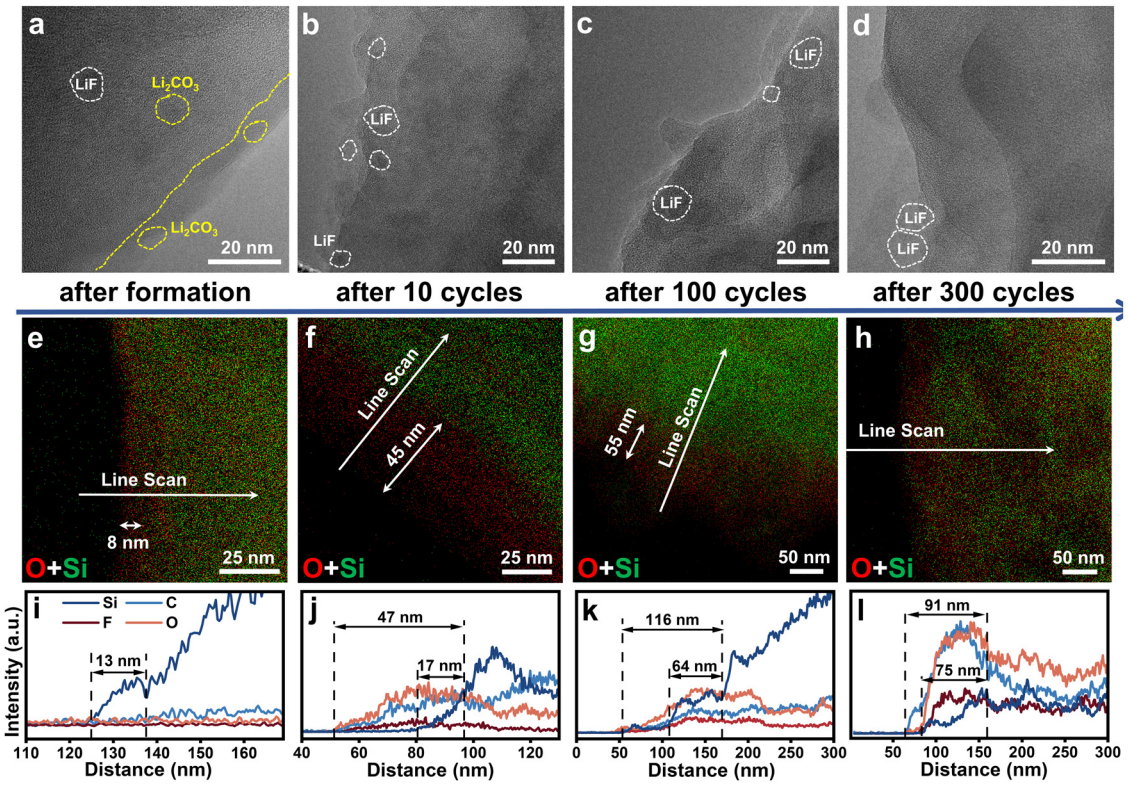

Fig. 4 Nanostructural evolution of the SEI on Si particles after different cycles. (a)–(d) HRTEM images, (e)–(h) distribution of O and Si, and (i)–(l) line-scanning elemental analysis of Si electrodes (a), (e) and (i) after formation, (b), (f) and (j) after 10 cycles, (c), (g) and (k) after 100 cycles, and (d), (h) and (l) after 300 cycles.

Cross profile of the SEI. To get a relatively complete interlayer from the Si particles after 300 cycles (Fig. 5), cryo-FIB was applied to prepare a cross-sectional lamella of the interlayer for TEM imaging. As shown in Fig. 5a, a porous interface layer is clearly present on the surface of the Si particle, which is about 200 nm thick and its porosity is estimated to be ~53.5%. From the surface to the bulk, four regions were selected for HRTEM imaging (Fig. 5b), and their nanostructures are displayed in Fig. 5c and Fig. S11–S14 (ESI†). Several crystalline Li_2O and LiF nanograins are located at the top surface of the interface layer. As aforementioned, Li_2O is prone to react with Si generating Li_xSiO_y, and the observed Li_2O is supposed to have formed when a thin layer of the SEI was present and shielding the Si particle while electrons can still tunnel through providing charge transfer for decomposition of organic solvents on the surface. The exterior part of the interface is found to be rich in LiF while its interior part is dominated by organic species, which is further confirmed by the elemental distribution of O (Fig. 5d), F (Fig. 5e), and Si (Fig. 5d and e). EELS spectra of O K-edge, Si $L_{2,3}$-edge, and C K-edge across the interface (Fig. 5f) provide another clue for the above observation, such as the existence of Li_2O (energy loss at ~535 eV, Fig. 5g) on the top surface. The interior interlayer mainly consists of amorphous Li_xSiO_y (energy loss at ~110 eV, Fig. 5h) and organic species (Fig. 5i) while the latter exhibits a stronger signal from the C–H bond (energy loss at ~288 eV, Fig. 5i) than that at the surface, indicating the potential incomplete decomposition of organic solvents due to the increased cell resistance after long cycles.

Growth mechanism of the SEI. According to the above observations and previous reports,[35] a comprehensive picture of the SEI growth mechanism on the Si particle during cycling can be proposed as shown in Fig. 6. It is first formed on the surface of the Si particle during the initial lithiation, consisting of some inorganic nanograins (*e.g.* Li_2O, LiF, and Li_2CO_3) and organic fragments. During the initial de-lithiation, along with the volume shrinkage of Si particles, some of the organic species in the SEI decompose releasing gases (*e.g.* CO_2, *etc.*) while Li_2O reacts with Si yielding amorphous $Li_2Si_2O_5$ or/and Li_2SiO_3; both contribute to forming pores in the SEI layer. The electrolyte continues to infiltrate through the SEI and reacts with the Si bulk, resulting in the bottom-up growth of SEI. Meanwhile, when the SEI is thin enough to allow electron tunneling, electrolytes can also be partially electrochemically decomposed on the top surface of the SEI, leading to the top-down growth of SEI. After that, the growth of the SEI layer is mainly dominated by the bottom-up growth mechanism, and its thickness continuously increases with the cycles, which can be up to micrometers after long cycles. Accumulation of the SEI not only consumes active Li^+ but also hinders interfacial Li^+ transport, resulting in a cell resistance increase and capacity degradation.

Given the intrinsic incompatibility and inevitable side reactions between the Si anode and the electrolyte, the presence of

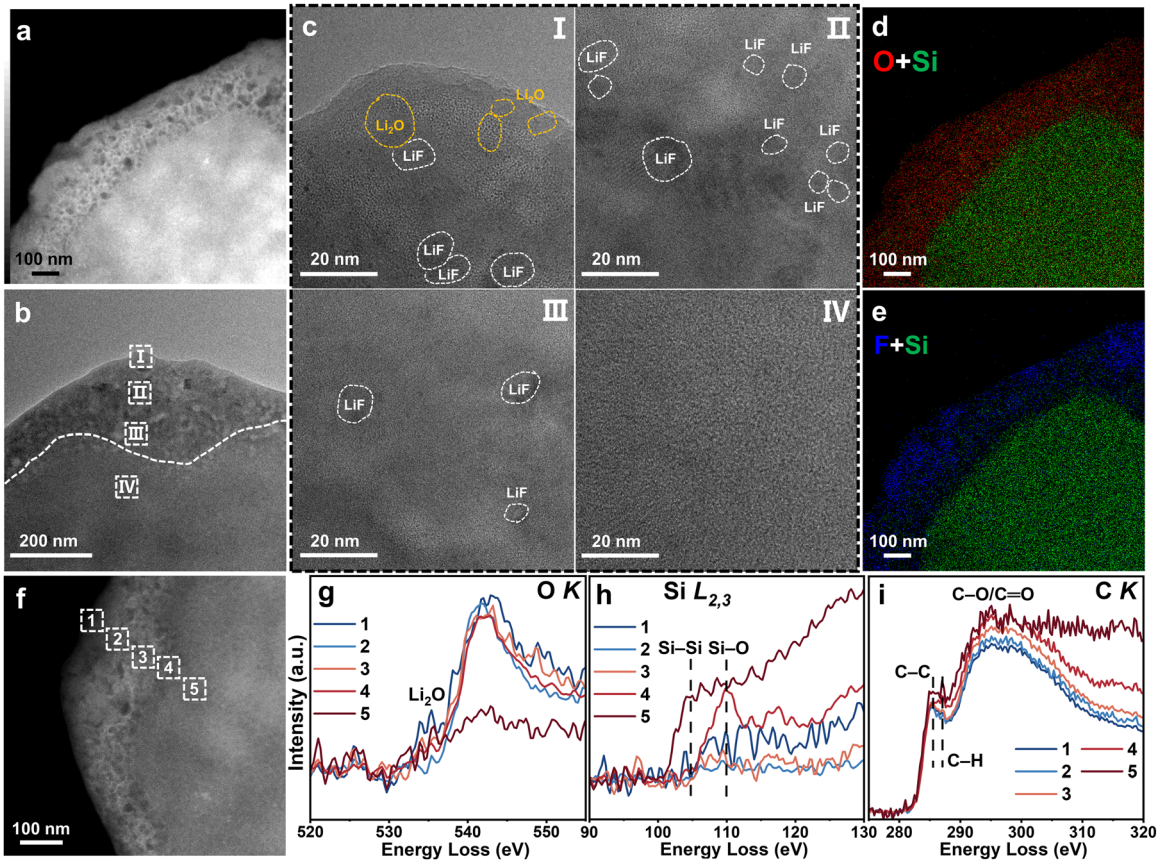

Fig. 5 Cross-profile of the SEI on the Si particles after 300 cycles. (a) STEM dark-field image of a lamella prepared by cryo-FIB. (b) TEM image and (c) its corresponding HRTEM images of some selected areas from the surface to the Si bulk. (d) and (e) Elemental distribution of O (in red), F (in blue), and Si (in green). (f) STEM dark-field image and (g)–(i) its corresponding EELS spectra of (g) O K-edge, (h) Si $L_{2,3}$-edge, and (i) C K-edge across the interface.

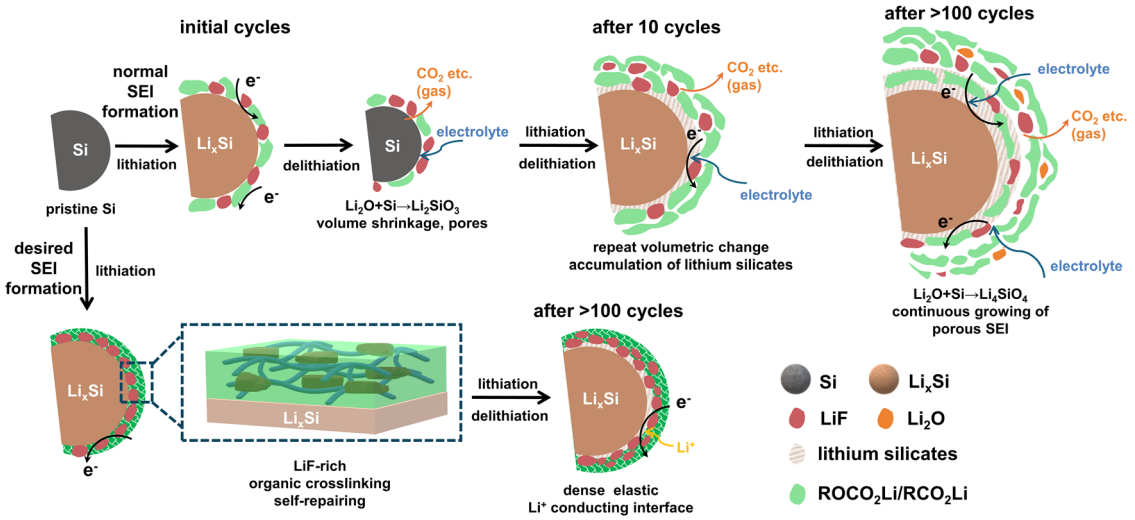

Fig. 6 Schematic illustration of the SEI growth on Si particles and the design principle of a desirable interface.

the SEI layer on the Si particles is expected to prevent their continuous side reactions. However, this task is difficult due to the porous nature of SEI, which allows electrolytes to infiltrate and corrode the Si bulk persistently. There are several reasons for the generation of pores in the SEI: (1) gas evolution involved in both SEI formation and decomposition, (2) instability of the SEI, including detachment, dissolution, reaction, and decomposition, (3) large volume changes, and (4) potential HF

corrosion. In this regard, besides the optimized electrolyte and particle nanostructure, a desirable SEI should be dense, elastic, and Li^+ conducting, and the SEI is not only rich in inert inorganic components but also requires crosslinking to tolerate the volumetric change. The former has been over-highlighted in the previous reports[47,48] while the latter has always been missed. As a proof of concept, an amount of sulfur is added to the electrolyte to initialize the polymerization and proved to be beneficial for improving the cycling performance of the Si anodes in both coin cells and pouch cells (Fig. S15–S17, ESI†).

Conclusions

In conclusion, characterization techniques from the electrode scale to the nanoscale were applied to investigate the degradation process of the Si anode from pouch cells. Besides the volume expansion of the Si electrode mainly during initial cycles (<10 cycles), continuous surface corrosion forming a thick SEI is responsible for the capacity loss of the Si anode. The micrometer-thick (2.5 μm after 300 cycles) SEI was profiled using cryogenic electron microscopy (cryo-EM) and exhibits a three-layered structure, which is dominated by organic species and Li_xSiO_y. The discrepancy of the nanoscale structure at different depths of the SEI layer suggests a pathway of bottom-up growth of the SEI due to its porous nature. Therefore, it is essential to build robust or elastic interfaces with cross-linking networks, especially during the initial cycles, to prevent aggressive SEI formation. The concept presented in this study reveals the degradation mechanism of the Si anode in pouch cells and provides a principle for a desirable SEI design for high-performance LIBs.

Author contributions

Q. F., X. W., and B. W. conceived the idea and designed the project. S. X., X. Z., and W. L. performed modification of the electrolyte for the Si anode. X. S. performed cryo-FIB to prepare the sample for cryo-TEM. D. L. performed SEM-Raman measurement. X. L. performed XPS measurement. Q. F. performed all other data collection and analysis. S. W., L. C., B. W., Z. W., X. W., and H. L. contributed to discussions and interpretation of results. Q. F., S. W., X. W., and B. W. co-wrote the manuscript, with input from all authors.

Data availability

The data supporting this article have been included as part of the ESI.†

Conflicts of interest

The authors declare no competing interests.

Acknowledgements

This work was supported by the National Key Research and Development Program of China (Grant No. 2022YFB2502200), the Beijing Municipal Natural Science Foundation (Grant No. Z200013), the China Postdoctoral Science Foundation (No. 2023M743739), the Postdoctoral Fellowship Program of CPSF (No. GZC20232939) and CAS Youth Interdisciplinary Team. The authors also thank the Beijing Clean Energy Frontier Research Center of the Institute of Physics of the Chinese Academy of Sciences and the Beijing office of Carl Zeiss (Shanghai) Co., Ltd for necessary characterization and analysis.

References

1 Y. Cui, *Nat. Energy*, 2021, **6**, 995–996.
2 K. Turcheniuk, D. Bondarev, G. G. Amatucci and G. Yushin, *Mater. Today*, 2021, **42**, 57–72.
3 G. G. Eshetu, H. Zhang, X. Judez, H. Adenusi, M. Armand, S. Passerini and E. Figgemeier, *Nat. Commun.*, 2021, **12**, 5459.
4 J. H. Ryu, J. W. Kim, Y.-E. Sung and S. M. Oh, *Electrochem. Solid-State Lett.*, 2004, **7**, A306–A309.
5 J. Li, X. Xiao, F. Yang, M. W. Verbrugge and Y.-T. Cheng, *J. Phys. Chem. C*, 2012, **116**, 1472–1478.
6 J. Xie, N. Imanishi, T. Zhang, A. Hirano, Y. Takeda and O. Yamamoto, *Mater. Chem. Phys.*, 2010, **120**, 421–425.
7 L. Y. Beaulieu, K. W. Eberman, R. L. Turner, L. J. Krause and J. R. Dahn, *Electrochem. Solid-State Lett.*, 2001, **4**, A137–A140.
8 M. T. McDowell, S. W. Lee, J. T. Harris, B. A. Korgel, C. Wang, W. D. Nix and Y. Cui, *Nano Lett.*, 2013, **13**, 758–764.
9 N. Kim, Y. Kim, J. Sung and J. Cho, *Nat. Energy*, 2023, **8**, 921–933.
10 M. N. Obrovac and L. Christensen, *Electrochem. Solid-State Lett.*, 2004, **7**, A93–A96.
11 Y. Yang, X. Qu, L. Zhang, M. Gao, Y. Liu and H. Pan, *ACS Appl. Mater. Interfaces*, 2018, **10**, 20591–20598.
12 F. Shi, Z. Song, P. N. Ross, G. A. Somorjai, R. O. Ritchie and K. Komvopoulos, *Nat. Commun.*, 2016, **7**, 11886.
13 U. Kasavajjula, C. Wang and A. J. Appleby, *J. Power Sources*, 2007, **163**, 1003–1039.
14 K. Tian, Z. Song, Q. Zhou, C. Guan, M. Lu, M. Zhang, D. Wei and X. Li, *J. Energy Storage*, 2023, **72**, 108401.
15 W. An, B. Gao, S. Mei, B. Xiang, J. Fu, L. Wang, Q. Zhang, P. K. Chu and K. Huo, *Nat. Commun.*, 2019, **10**, 1447.
16 N. Liu, Z. Lu, J. Zhao, M. T. McDowell, H.-W. Lee, W. Zhao and Y. Cui, *Nat. Nanotechnol.*, 2014, **9**, 187–192.
17 Q. Man, Y. An, C. Liu, H. Shen, S. Xiong and J. Feng, *J. Energy Chem.*, 2023, **76**, 576–600.
18 J. Sung, N. Kim, J. Ma, J. H. Lee, S. H. Joo, T. Lee, S. Chae, M. Yoon, Y. Lee, J. Hwang, S. K. Kwak and J. Cho, *Nat. Energy*, 2021, **6**, 1164–1175.
19 G. Qian, Y. Li, H. Chen, L. Xie, T. Liu, N. Yang, Y. Song, C. Lin, J. Cheng, N. Nakashima, M. Zhang, Z. Li, W. Zhao, X. Yang, H. Lin, X. Lu, L. Yang, H. Li, K. Amine, L. Chen and F. Pan, *Nat. Commun.*, 2023, **14**, 6048.

20 I. Yoon, D. P. Abraham, B. L. Lucht, A. F. Bower and P. R. Guduru, *Adv. Energy Mater.*, 2016, **6**, 1600099.
21 A. L. Michan, G. Divitini, A. J. Pell, M. Leskes, C. Ducati and C. P. Grey, *J. Am. Chem. Soc.*, 2016, **138**, 7918–7931.
22 S. Weng, Y. Li and X. Wang, *iScience*, 2021, **24**, 103402.
23 E. Zhang, M. Mecklenburg, X. Yuan, C. Wang, B. Liu and Y. Li, *iScience*, 2022, **25**, 105689.
24 W. Huang, J. Wang, M. R. Braun, Z. Zhang, Y. Li, D. T. Boyle, P. C. McIntyre and Y. Cui, *Matter*, 2019, **1**, 1232–1245.
25 X. Zhang, S. Weng, G. Yang, Y. Li, H. Li, D. Su, L. Gu, Z. Wang, X. Wang and L. Chen, *Cell Rep. Phys. Sci.*, 2021, **2**, 100668.
26 J. Quinn, B. Wu, Y. Xu, M. H. Engelhard, J. Xiao and C. Wang, *ACS Nano*, 2022, **16**, 21063–21070.
27 Y. He, L. Jiang, T. Chen, Y. Xu, H. Jia, R. Yi, D. Xue, M. Song, A. Genc, C. Bouchet-Marquis, L. Pullan, T. Tessner, J. Yoo, X. Li, J.-G. Zhang, S. Zhang and C. Wang, *Nat. Nanotechnol.*, 2021, **16**, 1113–1120.
28 Z. Lin, T. Liu, X. Ai and C. Liang, *Nat. Commun.*, 2018, **9**, 5262.
29 Y. Cao, M. Li, J. Lu, J. Liu and K. Amine, *Nat. Nanotechnol.*, 2019, **14**, 200–207.
30 M. Ue, K. Sakaushi and K. Uosaki, *Mater. Horiz.*, 2020, **7**, 1937–1954.
31 Q. Li, R. Yi, Y. Xu, X. Cao, C. Wang, W. Xu and J.-G. Zhang, *J. Power Sources*, 2022, **548**, 232063.
32 X. Chen, L. Li, M. Liu, T. Huang and A. Yu, *J. Power Sources*, 2021, **496**, 229867.
33 B. Sreenarayanan, D. H. S. Tan, S. Bai, W. Li, W. Bao and Y. S. Meng, *J. Power Sources*, 2022, **531**, 231327.
34 W. Bao, C. Fang, D. Cheng, Y. Zhang, B. Lu, D. H. S. Tan, R. Shimizu, B. Sreenarayanan, S. Bai, W. Li, M. Zhang and Y. S. Meng, *Cell Rep. Phys. Sci.*, 2021, **2**, 100597.
35 J. Kim, O. B. Chae and B. L. Lucht, *J. Electrochem. Soc.*, 2021, **168**, 030521.
36 P. Richet, B. O. Mysen and D. Andrault, *Phys. Chem. Miner.*, 1996, **23**, 157–172.
37 E. Radvanyi, E. De Vito, W. Porcher and S. Jouanneau Si Larbi, *J. Anal. At. Spectrom.*, 2014, **29**, 1120–1131.
38 K. W. Schroder, A. G. Dylla, S. J. Harris, L. J. Webb and K. J. Stevenson, *ACS Appl. Mater. Interfaces*, 2014, **6**, 21510–21524.
39 Y. Xu, H. Jia, P. Gao, D. E. Galvez-Aranda, S. P. Beltran, X. Cao, P. M. L. Le, J. Liu, M. H. Engelhard, S. Li, G. Ren, J. M. Seminario, P. B. Balbuena, J.-G. Zhang, W. Xu and C. Wang, *Nat. Energy*, 2023, **8**, 1345–1354.
40 R. E. Ruther, K. A. Hays, S. J. An, J. Li, D. L. Wood and J. Nanda, *ACS Appl. Mater. Interfaces*, 2018, **10**, 18641–18649.
41 Y. Yang, S. Yao, W. Liu, Y. Hu, Q. Li, Z. Li, S. Zhou and Z. Zhou, *Fuel Process. Technol.*, 2021, **213**, 106675.
42 A. Alemi and S. Khademinia, *Int. Nano Lett.*, 2015, **5**, 15–20.
43 K. Matsumoto, R. Hagiwara, Z. Mazej, E. Goreshnik and B. Žemva, *J. Phys. Chem. B*, 2006, **110**, 2138–2141.
44 R. Endo, T. Ohnishi, K. Takada and T. Masuda, *J. Phys. Chem. Lett.*, 2020, **11**, 6649–6654.
45 J. Fraxedas, M. Schütte, G. Sauthier, M. Tallarida, S. Ferrer, V. Carlino and E. Pellegrin, *Appl. Surf. Sci.*, 2021, **542**, 148684.
46 Y. Ma, Y. Zhou, C. Du, P. Zuo, X. Cheng, L. Han, D. Nordlund, Y. Gao, G. Yin, H. L. Xin, M. M. Doeff, F. Lin and G. Chen, *Chem. Mater.*, 2017, **29**, 2141–2149.
47 J. Chen, X. Fan, Q. Li, H. Yang, M. R. Khoshi, Y. Xu, S. Hwang, L. Chen, X. Ji, C. Yang, H. He, C. Wang, E. Garfunkel, D. Su, O. Borodin and C. Wang, *Nat. Energy*, 2020, **5**, 386–397.
48 J. Tan, J. Matz, P. Dong, J. Shen and M. Ye, *Adv. Energy Mater.*, 2021, **11**, 2100046.